



Experimental Study of Low-Thrust, End-Burning Solid Rocket Motors Including Plume Radiant Emission

Kelly J. Mathesius^{*}

Massachusetts Institute of Technology, Cambridge, Massachusetts 02139

Michael E. Knotts[†]

BAE Systems, Merrimack, New Hampshire 03054

and

Matthew T. Vernacchia[‡] and R. John Hansman[§]

Massachusetts Institute of Technology, Cambridge, Massachusetts 02139

<https://doi.org/10.2514/1.A36028>

Low-thrust, end-burning solid rocket motors have applications as propulsion systems for a class of small, transonic, uncrewed aerial vehicles. This paper provides new experimental measurements for characterizing small, low-thrust, end-burning motors. Four static fires measured the effects of motor chamber pressure and propellant oxamide content on exhaust plume radiant intensity, which could be important for vehicle visibility and tracking. Exhaust plume radiant intensity was found to be sensitive to a change in oxamide content and relatively insensitive to a change in chamber pressure for these motors. Thrust, chamber pressure, and burn rate were also measured for these motors, and a model for the minimum burn pressure of oxamide-doped propellants was improved.

Nomenclature

A_b	= propellant burn area, m ²
A_{LBB}	= laboratory blackbody radiating area, m ²
a	= propellant burn rate coefficient, mm s ⁻¹ MPa ⁻ⁿ
c^*	= propellant characteristic velocity, m s ⁻¹
$I_{b\lambda}$	= blackbody radiant intensity, W sr ⁻¹ m ⁻² μm ⁻¹
$J_{\lambda,plume}$	= exhaust plume radiant intensity, W sr ⁻¹ μm ⁻¹
K_λ	= radiometer response function, (counts per unit detector gain) · (W sr ⁻¹ m ⁻² μm ⁻¹) ⁻¹
L	= distance from radiometer to target, m
n	= propellant burn rate exponent, -
P_c	= chamber pressure, Pa or MPa
r	= propellant burn rate, mm s ⁻¹
S	= measured signal from radiometer, (counts per unit detector gain)
T	= temperature, K
w_{om}	= propellant oxamide mass fraction, -
λ	= wavelength, μm or burn rate model parameter, -

Subscripts

b	= burning surface
LBB	= laboratory blackbody
LBB_bg	= background of laboratory blackbody
$plume$	= plume
$plume_bg$	= background of plume
λ	= spectral quantity

I. Introduction

LOW-THRUST, long-burn-time solid rocket motors could be used as propulsion systems for a class of small, transonic uncrewed aerial vehicles (UAVs). Motors with these characteristics can be achieved with end-burning grains to reduce burn area, low-operating chamber pressures, or large oxidizer particle sizes or a burn rate suppressant to reduce the propellant burn rate [1]. Several previous works have used these principles. JPL tested a series of long-endurance motors, which operated at low chamber pressure (≤ 1.0 MPa) and produced ~ 8 kN thrust for 110 to 138 s [2]. Nowakowski et al. proposed a 44 kg end-burning propellant grain with a thrust of 245 N and a burn time of 324 s for space debris mitigation applications [3]. The Atlantic Research Corporation developed the Five-Minute Rocket Motor for aircraft propulsion applications, which used an end-burning grain and chamber pressure of 2.4 MPa to produce 200 N thrust for 290 s [4]. A survey of other studies looking at low-burn-rate solid rocket motors is available in Ref. [5].

The motors considered in this study are significantly smaller and are compatible with a low-thrust aircraft concept proposed by Vernacchia et al. [6], which is illustrated in Fig. 1. It uses a kilogram-scale, end-burning, long-burn-time motor with a case diameter of 65 mm that provides 5 to 10 N thrust for 1 to 3 min. The propellants are a class of oxamide-doped ammonium perchlorate composite propellants, which use 0 to 20% of the burn rate suppressant oxamide and have experimentally measured burn rates of 1 to 4 mm s⁻¹ at a chamber pressure of 1 MPa [7].

This study measured exhaust plume infrared radiant emission for such motors, which could be important for vehicle visibility and tracking for the previously described aircraft concept. Several other previous studies have experimentally measured exhaust plume infrared radiant emission from solid rocket motor exhaust plumes [8–11]. However, to the authors' knowledge, no study in the open literature has measured exhaust plume radiant emission for very low-thrust (<20 N) motors or for motors with solid propellants doped with oxamide.

The small size, low combustion and nozzle exit temperatures, and low mass flow rates of these motors lead to radiant emission phenomena that are distinct from larger motors with higher mass flow rates. Given the very small size, it is expected that the afterburning reaction timescale is much slower than the plume transit timescale, and therefore no afterburning is present (a phenomenon mentioned briefly by Rudman and Hibbeln [12] and Kim et al. [11] and discussed in more detail in ch. 8 of Ref. [13]). Additionally, the small

Received 11 February 2024; revision received 12 June 2024; accepted for publication 29 June 2024; published online 9 August 2024. Copyright © 2024 by the authors. Published by the American Institute of Aeronautics and Astronautics, Inc., with permission. All requests for copying and permission to reprint should be submitted to CCC at www.copyright.com; employ the eISSN 1533-6794 to initiate your request. See also AIAA Rights and Permissions www.aiaa.org/randp.

*Graduate Researcher, Department of Aeronautics and Astronautics, kjmath@mit.edu. (Corresponding Author).

†Scientist Senior Principal III, FAST Labs.

‡Visiting Scientist, Plasma Science and Fusion Center.

§T. Wilson Professor in Aeronautics, Department of Aeronautics and Astronautics. Member AIAA.

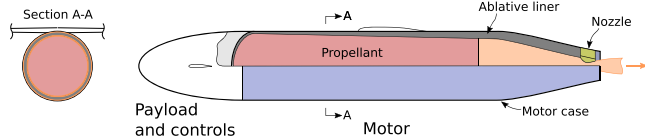


Fig. 1 Configuration for a small, low-thrust UAV proposed by Vernacchia et al. uses an end-burning solid rocket motor. Reproduced from Ref. [6].

size can lead to a plume that is optically thin across the infrared spectrum, unlike larger motors which are typically optically thick (at least in the $4.3\text{ }\mu\text{m}$ CO_2 and $2.7\text{ }\mu\text{m}$ H_2O and CO_2 bands). These phenomena lead to significantly reduced temperatures throughout the exhaust plume and a radiant emission from this class of motors that is less than might be anticipated by the reduced size alone. Experimental measurements for plumes of this small size are important for benchmarking the performance of this unique class of motors and for informing future design of aircraft with low-thrust, end-burning rocket motors.

Static fire experiments for this research used motors that were operated at chamber pressures of approximately 1.1 or 2.2 MPa with ammonium perchlorate composite propellants that were doped with 0 or 8% oxamide. In addition to exhaust plume radiant intensity measurements, motor thrust, chamber pressure, and burn rates were measured, and the new results were used to improve a model for the minimum burn pressure of oxamide-doped propellants originally proposed by Vernacchia et al. [7]. The exhaust plume radiant emission data from this work were used to validate an end-to-end differentiable model for plume radiant emission compatible with gradient-based optimizers discussed in an accompanying paper [14].

II. Test Motor

A. Motor Design

A consistent end-burning motor configuration was used for these experiments. A rendering of the motor design is given in Fig. 2. The motor case and closure material was 316 stainless steel, and the insulator material was phenolic composite. All motors had a burning area of 1140 mm^2 . The motor used a swappable nozzle insert made from a machinable alumina-silicate material with an expansion half-angle of 15° and an expansion area ratio optimized for sea level pressure. For the four static fires described in this paper, the nozzle was water-cooled to ensure reasonable temperatures were maintained in the aft closure.

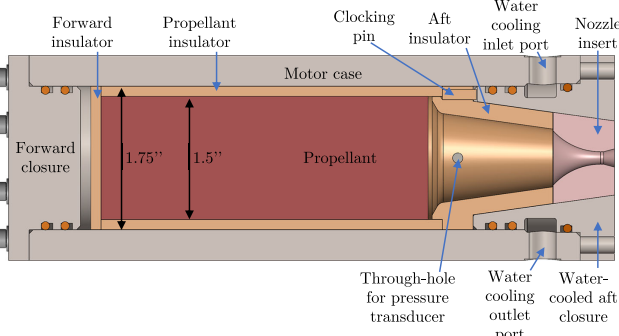


Fig. 2 End-burning test motor design.

B. Propellants

1. Propellant Formulation

Two different ammonium perchlorate composite propellant formulations were used: a *baseline* formulation and formulation with 8% oxamide. The baseline propellant formulation for these experiments is shown in Table 1. It is an ammonium perchlorate and hydroxyl terminated polybutadiene propellant and was previously characterized by Vernacchia et al. [7]. To create the 8% oxamide formula, the baseline propellant formulation is diluted with the desired mass fraction of the additive. If a mass fraction w_{om} of oxamide is desired, then the new propellant formulation is created by scaling the mass fractions in Table 1 by a factor of $1 - w_{\text{om}}$, and then w_{om} oxamide is added.

2. Propellant Combustion Products

The combustion products of the baseline propellant doped with 0 and 8% oxamide were computed and are given in Table 2. A custom thermodynamic equilibrium code—described in Ref. [14] and validated using outputs from the commercial Rocket Propulsion Analysis [15] solver—was used for calculating these values. Including oxamide in the propellant formulation does not create any significant quantities of new combustion products that were not already present in the 0% oxamide propellant, as shown in Table 2.

3. Propellant Manufacturing

Propellant grain manufacturing was completed in several steps. The oxidizer, opacifier, and burn rate suppressant were premeasured. The binder and plasticizer were measured and mixed by machine for several minutes, and then the opacifier and burn rate suppressant were added and mixed until incorporated. The oxidizer was then added slowly while the mixer was running. Once the oxidizer was incorporated, vacuum was pulled on the mixing bowl and the propellant was mixed under vacuum for 2 h at a speed of ~ 30 rpm. Lastly, the curative was added to the mixing bowl through a valve in the mixer lid, and the propellant was mixed for an additional 10 min to incorporate the curative. All propellant components were measured by weight. The propellant was mixed in a custom vacuum mixer made from a heavily modified Bosch Universal Plus MUM6N10 kitchen mixer with a $\sim 6.2\text{ L}$ capacity. Additional details regarding the propellant mixing process and the custom vacuum mixer can be found in Ref. [16].

After the propellant was mixed, the propellant was packed directly into precut, primed off-the-shelf phenolic composite tubes, which also served as the propellant insulating liner as described in Sec. II.A. The primer was hydroxyl-terminated polybutadiene rubber based

Table 2 Equilibrium combustion products assuming 1 MPa chamber pressure for oxamide mass fractions of 0 and 8%

Species	0% oxamide		8% oxamide	
	Mole fractions	Mass fractions	Mole fractions	Mass fractions
CO	0.251	0.319	0.259	0.337
CO_2	0.055	0.111	0.056	0.114
H_2	0.217	0.020	0.241	0.023
H_2O	0.250	0.205	0.220	0.184
HCl	0.149	0.248	0.135	0.228
N_2	0.076	0.097	0.088	0.115

Columns do not sum exactly to 1 due to rounding and existence of trace species.

Table 1 Baseline propellant formulation

Ingredient	Chemical name	Manufacturer	Mass fraction
Binder	Hydroxyl terminated polybutadiene (HTPB) resin with HX-752 and CAO-5	RCS rocket motor components	0.125
Plasticizer	Isodecyl pelargonate (IDP)	RCS rocket motor components	0.052
Opacifier	Graphite powder	Cretacolor	0.003
Oxidizer	Ammonium perchlorate 400 μm blend	RCS rocket motor components	0.800
Curative	Modified MDI isocyanate	RCS rocket motor components	0.020

and was formulated with an excess of curative to ensure there were plenty of available reactive groups to bond with the propellant (see Appendix A.1 of Ref. [13] for more details). Many propellant grains were cast from each propellant mix. All propellant grains were imaged with x-rays to inspect for voids or other defects within the grain. Propellants grains with significant voids were not used, because the voids would have likely resulted in unpredictable propellant burning areas and motor chamber pressures.

C. Motor Ignition

One of two ignition primers was used in the static fires. Either a small piece ($\sim 1 - 2\text{ g}$) of a faster burning commercial propellant (CTI Classic propellant) was adhered onto the surface of the main motor grain with polyurethane adhesive, or the surface of the grain was coated with a commercial pyrogen coating (QuickBurst QuickDip coating). Both ignition primers were ignited with a 6 W 450 nm laser.

III. Measurement Methods

A. Test Setup and Instrumentation

The motor test setup is shown in Fig. 3. The motors were mounted to a thrust stand positioned in front of a wall painted with a high-emissivity paint (Krylon Ultra Flat Black 1602 spray paint). Thrust, chamber pressure, and exhaust plume radiant emission measurements were collected for each motor. An exhaust duct was positioned downstream of the motor to collect the exhaust and vent it outside. This ventilation helped to prevent the exhaust gases from stagnating downstream of the motor and potentially obstructing the exhaust plume radiant emission measurement.

The radiant emission measurements were collected using a CI Systems SR-5000N spectroradiometer. The radiometer used liquid nitrogen cooled indium–antimonide and mercury–cadmium–telluride photovoltaic detectors that together are sensitive to radiation from 1.2 to 14.2 μm . A continuous variable filter sampled the different wavelengths during measurements into 379 wavelength bins across the spectrum. A 18.7° field of view was used, and the spectrum was scanned at a rate of 1 Hz at the maximum instrument gain setting. Measurements were made relative to a floating internal blackbody in the radiometer.

The spectroradiometer was kept in an enclosure with an optical window in front of the detector. An uncoated zinc sulfide window was used for Static Fire 1 (SF-1) and SF-2, and an uncoated calcium fluoride window was used for SF-3 and SF-4. The position of the radiometer relative to the test motor is shown in Fig. 4.

Thrust was measured using an Omega LCEB-5 load cell with a rated capacity of 5 lbf (22 N). The load cell was connected to a swung platform on a specialized thrust stand on which the motor was mounted, which is described in greater detail in sec. 7.3 of Ref. [17]. Chamber pressure was measured using an Omega PX119-600AI pressure transducer with a 600 psi (4.1 MPa) maximum pressure. Burn rate was calculated with two different methods—an *average burn rate method* and a c^* -based *burn rate method*—from pressure and burn-time data. The procedures for these two methods are given in Appendix A of Ref. [17].

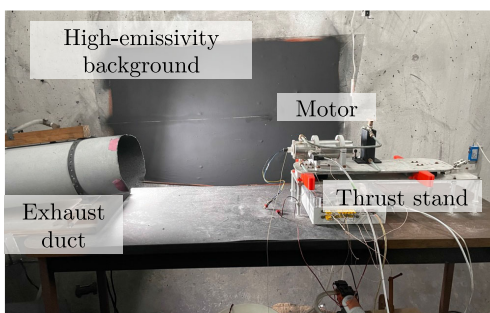


Fig. 3 Test motor mounting and exhaust system.

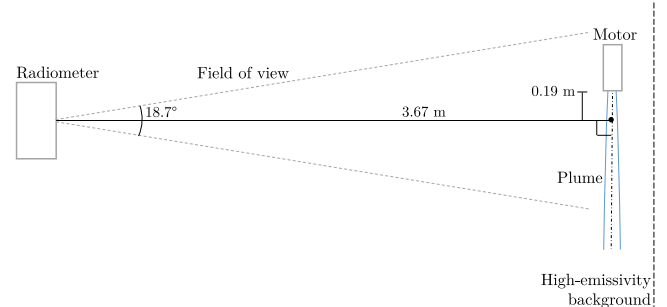


Fig. 4 Positioning of motor relative to radiometer and background.

B. Data Processing for Radiant Intensity

Four different radiometric measurements were collected for each motor static fire to determine the exhaust plume radiant intensity in units of $\text{W sr}^{-1} \mu\text{m}^{-1}$. For each static fire, the four collected radiation measurements were of the following:

- 1) S_{plume} : the exhaust plume, including all of the background within the field of view
- 2) $S_{\text{plume_bg}}$: the background of the exhaust plume without the motor burning
- 3) S_{LBB} : a calibrated laboratory blackbody with a known temperature T_{LBB} , aperture area A_{LBB} , and distance to detector L_{LBB}
- 4) $S_{\text{LBB_bg}}$: the background of the laboratory blackbody (i.e., a measurement of the laboratory blackbody with the aperture covered); this measurement is nearly identical to the background of the exhaust plume $S_{\text{plume_bg}}$ ^{**}

The measurements for S_{LBB} and $S_{\text{LBB_bg}}$ were used to calculate a response function K_λ to translate from detector units of *counts per unit detector gain* to units of $\text{W sr}^{-1} \text{m}^{-2} \mu\text{m}^{-1}$:

$$K_\lambda \equiv \frac{S_{\text{LBB}} - S_{\text{LBB_bg}}}{(A_{\text{LBB}}/L_{\text{LBB}}^2)[I_{b\lambda}(T_{\text{LBB}}) - I_{b\lambda}(T_{\text{LBB_bg}})]} \quad (1)$$

The response function was then used to determine exhaust plume radiant intensity from S_{plume} and $S_{\text{plume_bg}}$:

$$J_{\lambda,\text{plume}} \approx L_{\text{plume}}^2 \frac{S_{\text{plume}} - S_{\text{plume_bg}}}{K_\lambda} \quad (2)$$

where L_{plume} is the distance from the detector to the plume. For the experiments, $L_{\text{plume}} = L_{\text{LBB}} = 3.67 \text{ m}$.

Each of the four spectral radiation measurements collected for each motor static fire was actually a collection of individual scans from the radiometer, which scanned the spectrum at a rate of 1 Hz. For each measurement, all suitable scans collected were averaged for each wavelength, but were otherwise not filtered. The averaged measurements were used in Eqs. (1) and (2) for determining exhaust plume spectral radiant intensity.

The measurements for the plume and plume background were collected in the same radiometer scan run starting 60 s before motor ignition and continuing through the motor burn. The scans comprising the background and plume measurement were determined through simple visual inspection of the raw detector signal at each scan at 4.298 μm wavelength, which is the wavelength corresponding to CO₂ emission and has the largest signal. The plume measurement only included scans where the motor was burning at steady state (so excluding any peaks at startup).

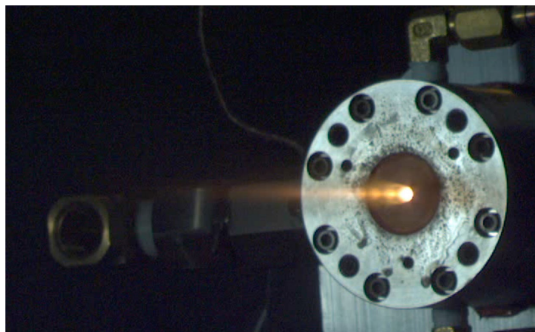
IV. Experimental Results and Discussion

Four static fires of the test motor are discussed in this section. The motors were tested with two different oxamide contents (0 and 8%, as discussed in Sec. II.B) and two different chamber pressures

^{**} $S_{\text{LBB_bg}}$ was not collected separately for static fire SF4, and so $S_{\text{plume_bg}}$ was substituted

Table 3 Summary of the test motor firings discussed in this section

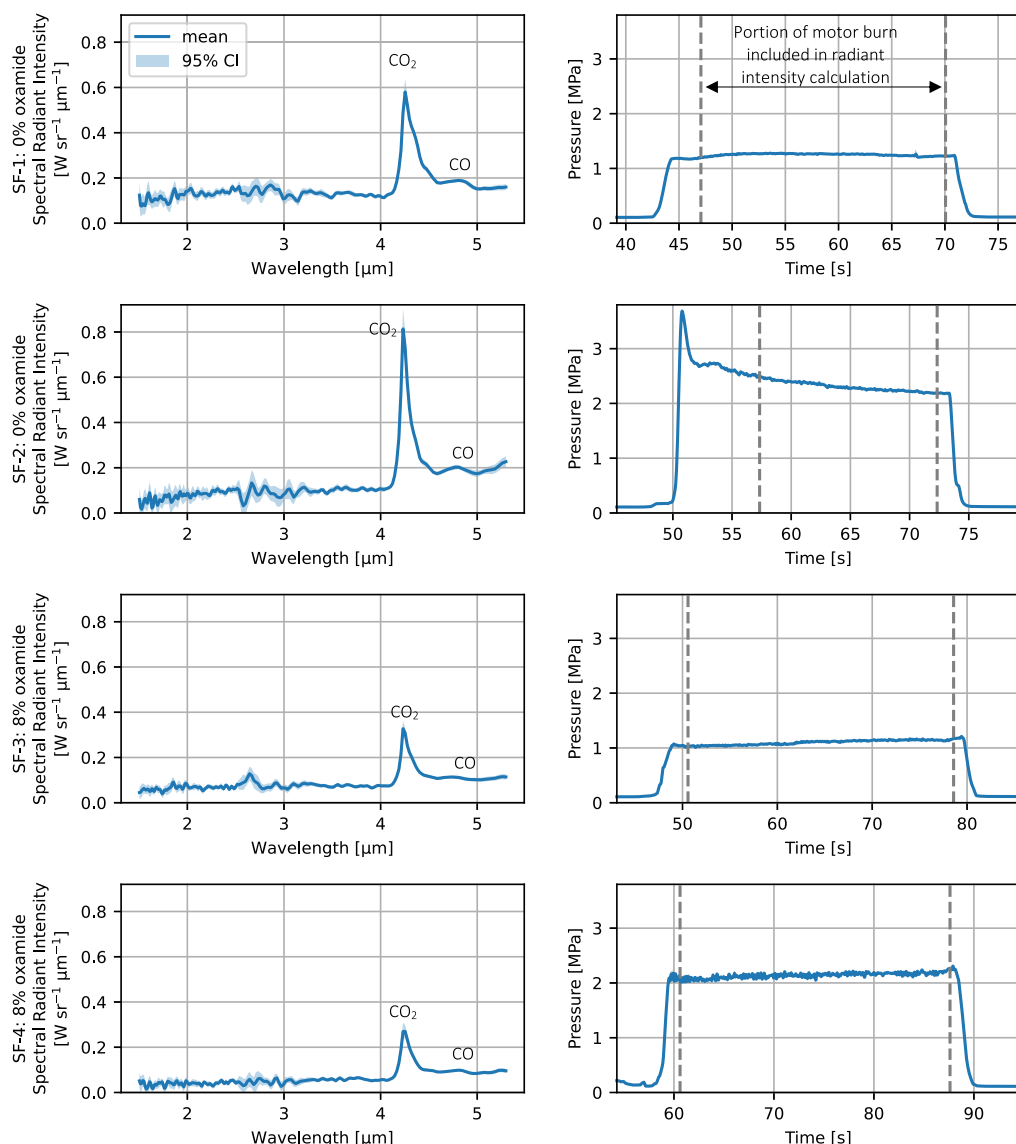
Static fire	Oxamide, %	Ignition primer	Burn length, mm	Throat diameter, mm	Burn time, s	Mean steady chamber pressure (± 1 SD), MPa	Mean steady thrust (± 1 SD), N	Mean radiant intensity at 4.3 μm CO_2 peak ($\pm 95\%$ CI), $\text{W sr}^{-1} \mu\text{m}^{-1}$	# of radiant intensity scans
SF-1	0	Coating	86.2	3.00	27.5	1.25 ± 0.02	9.58 ± 0.20	0.58 ± 0.06	24
SF-2	0	Grain	86.2	2.30	23.6	2.31 ± 0.08	12.55 ± 0.22	0.81 ± 0.09	16
SF-3	8	Coating	67.3	2.53	32.1	1.10 ± 0.04	6.13 ± 0.15	0.31 ± 0.03	29
SF-4	8	Coating	67.2	1.93	29.9	2.14 ± 0.05	7.30 ± 0.10	0.27 ± 0.03	28

**Fig. 5** Visible portion of a static fire exhaust plume.

(~1.1 MPa and ~2.2 MPa). These tests are summarized in Table 3. A visible image of a static fire exhaust plume is shown in Fig. 5. The visible portion of the exhaust plume is less than 1 cm in diameter and is approximately 5 cm in length.

A. Exhaust Plume Radiant Intensity and Chamber Pressure

The radiant intensity and chamber pressure measurements for these motors are shown in Fig. 6. The pressure traces for SF-1, SF-3, and SF-4 were relatively flat, which is the desired behavior for an end-burning motor. SF-2 showed an initial peak in pressure, which eventually decayed to a relatively steady chamber pressure, although the trace was still slightly regressive. The peak and decay were most likely due to the use of a relatively large starter grain for igniting the

**Fig. 6** Exhaust plume spectral radiant intensity and chamber pressure measurements for test motors.

propellant (the other static fires used an ignition coating instead, as indicated in Table 3). This starter grain created an initial increase in burning area before being consumed, which explains the initial peak in chamber pressure. It's possible that the hotter, faster burning commercial propellant starter grain caused the main propellant grain near the starter grain to momentarily burn faster than the rest of the propellant surface, altering the propellant surface geometry such that the rest of the pressure profile was slightly regressive.

The spectra in the left subplots of Fig. 6 are the average of spectral measurements taken at a rate of 1 Hz during the steady-pressure phase of the motor firing (indicated by dashed gray vertical lines on the right subplots). The spectra plots also show the calculated 95% confidence intervals for the mean spectral radiant intensity at each wavelength. (The number of available scans used for calculating the confidence interval for each static fire is given in Table 3.)

The measurements for each motor test are slightly noisy. Measuring the radiant emission of these small, slow-burning solid rocket motors required operating the spectroradiometer near its lower sensitivity limit. Even at the maximum gain setting, the exhaust plume contrast measurements used, at most (at the $4.3\text{ }\mu\text{m}$ CO_2 band where the signal was strongest), 7.7% of the dynamic range of the detector.

Emission bands in the radiant intensity spectra for the motors correspond to the combustion products in the motor exhaust, which are given in Table 2. The radiant intensity spectra for SF-1 to SF-4 each had a strong peak at $4.3\text{ }\mu\text{m}$. This peak was due to the CO_2 in the exhaust plume, which has a strong molecular emission band centered at $4.3\text{ }\mu\text{m}$. A weaker peak at $4.7\text{ }\mu\text{m}$ can also be seen, which is due to CO emission. For a larger motor with more emission, a band centered at $2.7\text{ }\mu\text{m}$ due to both H_2O and CO_2 and a band centered at $3.5\text{ }\mu\text{m}$ for HCl would be expected, given the expected combustion products in the motor's exhaust. However, these weaker emission bands were not very pronounced for these small, low-thrust motors. H_2 and N_2 do not emit in the infrared at the prevailing plume temperatures, so it is expected that there are no emission peaks for these exhaust products ([18] sec. 3.1). Additionally, the soot mass fraction in these plumes is minimal, with a measured value of 0.0135 for these propellants [6]. The soot adds a very low magnitude, continuous emission across the spectrum, which at these concentrations, temperatures, and size scales is not discernible from measurement noise. As mentioned in Sec. II.A, an exhaust system extracts smoke and exhaust products from the test cell to ensure they do not stagnate downstream of the motor and obstruct the radiant emission measurement.

The intensities of the $4.3\text{ }\mu\text{m}$ CO_2 emission peak for SF-1 to SF-4 are compared in Fig. 7 (again, the plot shows the mean and 95% confidence interval of several spectral measurements taken during the steady-pressure phase of the firing). The difference in peak spectral radiant intensity due to the change in oxamide content was greater than that due to the change in chamber pressure. For the 0% oxamide

motors (SF-1 and SF-2), the increase of chamber pressure from $\sim 1.2\text{ MPa}$ to $\sim 2.3\text{ MPa}$ led to a $\sim 40\%$ increase in peak spectral radiant intensity. For the 8% oxamide propellant (SF-3 and SF-4), the increase in chamber pressure from $\sim 1.1\text{ MPa}$ to $\sim 2.1\text{ MPa}$ led to a $\sim 12\%$ decrease¹. For motors operating near $\sim 1.1\text{ MPa}$ (SF-1 and SF-3), increasing propellant oxamide content from 0 to 8% led to a 47% decrease in peak radiant intensity; for motors operating near $\sim 2.2\text{ MPa}$ (SF-2 and SF-4), increasing the oxamide content led to a 67% decrease.

B. Thrust

The thrust measurements for these motors are shown in Fig. 8. Like the pressure traces in Fig. 6, the thrust traces were also relatively flat, which was expected given the end-burning motor configuration. Also like the pressure trace for SF-2, there was a peak in the thrust on motor startup due to the use of a larger starter grain for this motor. Stiction in

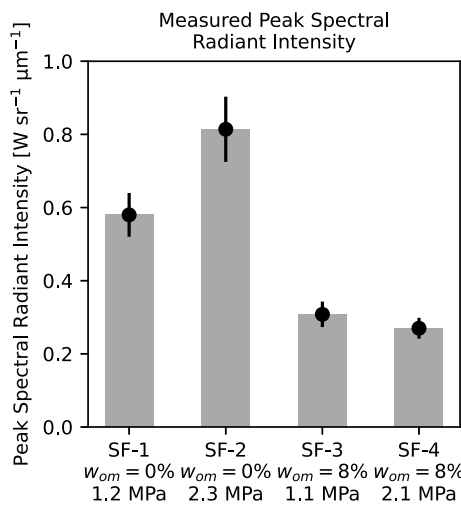


Fig. 7 Comparison of mean peak spectral radiant intensities for different motor test firings, with 95% confidence intervals.

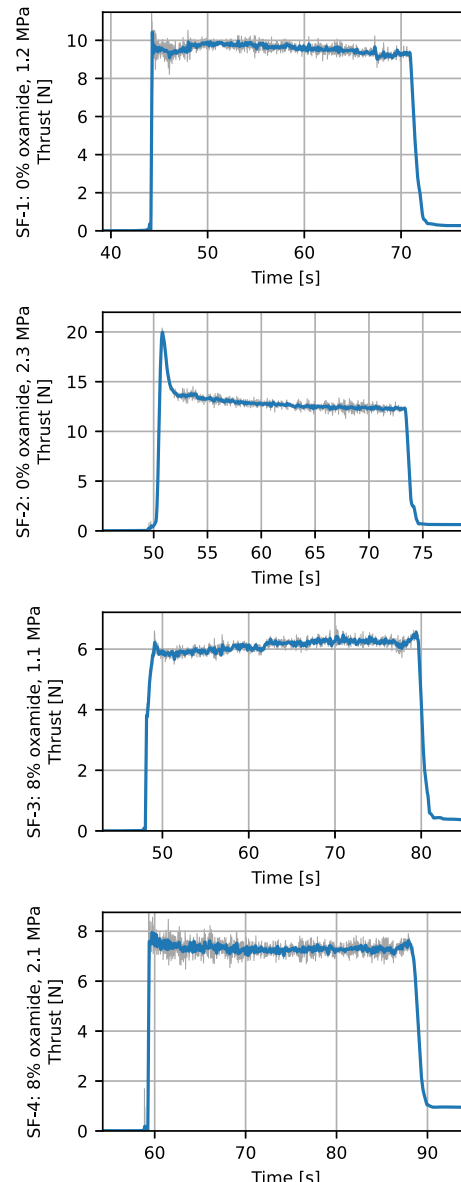


Fig. 8 Thrust curves for test motors. Gray curves are the raw measurements, and blue curves are filtered by a 5 Hz lowpass symmetric Butterworth filter.

¹Although the 95% confidence intervals for SF-3 and SF-4's intensity overlap, a *t*-test on the null hypothesis "the intensity measurements for SF-3 and SF-4 were drawn from populations with the same mean" has a *p*-value of 0.012.

the thrust stand due to a small amount of rubbing between the thrust stand swung platform and flexures caused the thrust measurements to not return all the way to zero after the thrust load was removed. As anticipated, thrust was higher for motors with higher chamber pressure and propellant with lower oxamide content.

C. Burn Rate

The burn rate of composite propellants is typically modeled using an empirical burn rate law:

$$r = ap_c^n \quad (3)$$

where r is the propellant burn rate, a is the burn rate coefficient, n is the burn rate exponent, and p_c is the chamber pressure. The burn rate coefficient and exponent (a and n) are typically measured experimentally for a given propellant. Two methods were used for determining the burn rate coefficients in this work: an *average burn rate* method and a c^* -based method. These methods are described in detail in Appendix A.2 of Ref. [17]. For oxamide-doped propellants, Vernacchia et al. developed a theoretical burn rate law which predicts the burn rate coefficient a for a propellant that is diluted with some mass fraction w_{om} of the burn rate suppressant oxamide, given the burn rate coefficient $a_{w_{om}=0}$ for the undoped propellant [7]:

$$a(w_{om}) = a_{w_{om}=0} \frac{1 - w_{om}}{1 + \lambda w_{om}} \quad (4)$$

The burn rate coefficient n does not change with oxamide content, which is supported by the data in Ref. [7]. The dimensionless parameter λ is a function of gasification enthalpies for oxamide and the undoped propellant and has a value of $\lambda \approx 6.20$ for propellants in this work and in Ref. [7].

A plot of the measured burn rate coefficients for this work, as well as the measured burn rate coefficients and the burn rate model from Ref. [7], are shown in Fig. 9. The burn rate coefficient model from Ref. [7] overpredicts the burn rate for the static fires completed in this work: the measurements from this work are ~ 20 to 25% less than the model. This overprediction could be due to the difference in motor designs between the motor in this work, discussed in Sec. II.A, and the motor design used in Ref. [7], which had a slightly larger burning surface area (1140 mm^2 for this work and 1257 mm^2 for Ref. [7]) and a much thinner motor case (9.5 mm thick for this work and 1.6 mm thick for Ref. [7]). The smaller burn area and larger heat capacity of the motor case for the motor used in this work could have resulted in greater thermal losses to the motor case walls as compared

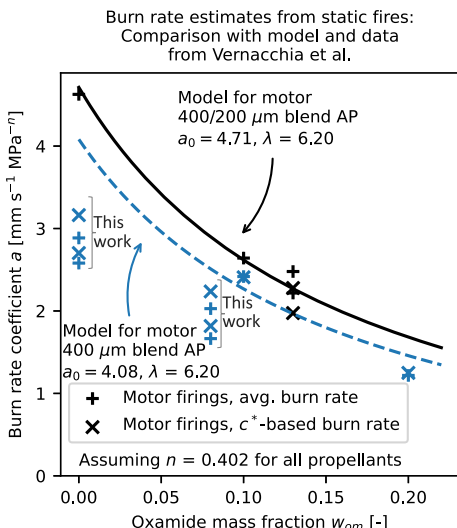


Fig. 9 Comparison of the measured burn rate coefficients for the static fires given in Fig. 3 with the model and static fire measurements published in Ref. [7].

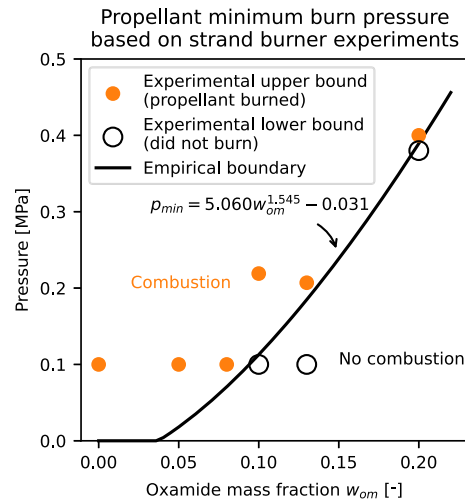


Fig. 10 Minimum burn pressure data for the class of propellants used in this work originally published in Ref. [7], along with the addition of the data point at $w_{om} = 0.08$ from this work.

to the motors in Ref. [7], which would have the effect of slowing down the propellant burn rate.

D. Minimum Burn Pressure

The family of propellants used in this work has a minimum burn pressure below which the propellant cannot stably burn. The minimum burn pressure was previously characterized for oxamide-doped propellants by Vernacchia et al. in Ref. [7]. In that work, ignition of propellants containing 0, 5, 10, 13, and 20% oxamide was attempted at various pressures at or above atmospheric pressure. A quadratic minimum burn pressure model was then fit to the ignition data as a function of oxamide content.

The original data and model in Ref. [7] suggested that the oxamide content where the propellant transitioned from unsuccessful to successful combustion at standard pressure (0.101 MPa) was between 5 and 10%. Because testing propellant ignition at pressures below atmospheric pressure is difficult, reducing the known transition oxamide range at standard pressure is desirable as a relatively simple way to improve the accuracy of the model. Subsequently, ignition of 8% oxamide propellant mixed for this work was attempted at standard pressure, and it was found to burn stably. This new ignition data point, as well as the data given in Ref. [7], are shown in Fig. 10.

An updated empirical boundary for the minimum burn pressure was also determined, which is also given in Fig. 10. As noted in Ref. [7], the choice of a quadratic dependence on oxamide content was arbitrary, and there was no theoretical basis for it. For this work, a power law with constant offset model was used to fit the data. This model, like the quadratic, still has three fitted parameters. However, for this model the exponent was among the fitted parameters (it has a fitted value of 1.545, as shown in Fig. 10), which perhaps provides more intuition for the true dependence of minimum burn pressure on oxamide content than the quadratic model.

V. Conclusion

The measurements presented in this paper can be used for improving the design of low-thrust, end-burning rocket motors and small, transonic UAVs. Experimental static fires of low-thrust, end-burning motors were conducted to measure exhaust plume radiant emission, chamber pressure, thrust, and burn rate. The static fire motors were operated with either 0 or 8% oxamide and at a chamber pressure of approximately 1.1 or 2.2 MPa.

For the exhaust plume radiant intensity measurements, the strongest emission in the measured spectrum for all the motors occurred at $4.3 \mu\text{m}$, corresponding to CO_2 emission. From the radiant intensity measurements, it appears that the radiant intensity is sensitive to changes in propellant oxamide content and relatively insensitive to changes in motor operating chamber pressure. To the authors' knowledge, the

measurements collected in this work represent the lowest thrust levels for which rigorous plume radiant intensity measurements have been obtained and the only plume radiant intensity measurements for propellants containing oxamide in the open literature.

The static fires also measured the effects of oxamide content and chamber pressure on thrust and burn rate. As anticipated, the addition of oxamide reduced the motor thrust and burn rate. A previous model for burn rate of oxamide-doped propellants given by Vernacchia et al. predicted slightly faster burn rates than were measured in this study, but this is likely explained by the significantly larger thermal mass of the motor case used in this work. Additionally, a minimum burn pressure model for oxamide-doped propellants was revised with measurements from this work, which is useful for the design of low-pressure motors.

Acknowledgments

This work was funded by BAE Systems, Inc. The authors thank MIT undergraduate researchers Jorian Benke and Tamara Hinderman for their assistance in propellant manufacturing and static fire test operation.

References

- [1] Sutton, G. P., and Biblarz, O., *Rocket Propulsion Elements*, 8th ed., Wiley, Hoboken, NJ, 2010, pp. 435–536, Chaps. 12–13.
- [2] Shafer, J. I., “Solid-Propellant Motors for High-Incremental-Velocity Low-Acceleration Maneuvers in Space,” 1972, <https://ntrs.nasa.gov/search.jsp?R=19720012197>.
- [3] Nowakowski, P., Kasztankiewicz, A., Marciniak, B., Okninski, A., Pakosz, M., Noga, T., Majewska, E., Rysak, D., and Wolanski, P., “Space Debris Mitigation Using Dedicated Solid Rocket Motor,” *8th European Conference for Aeronautics and Space Sciences*, Paper EUCASS2019-994, 2019. <https://doi.org/10.13009/EUCASS2019-994>
- [4] Compton, J., Thies, C., Kurzeja, S., and McGarry, J., “Five-Minute Rocket Motor,” *AIAA/SAE 10th Propulsion Conference*, AIAA Paper 1974-1203, 1974. <https://doi.org/10.2514/6.1974-1203>
- [5] Okniński, A., Nowakowski, P., and Kasztankiewicz, A., “Survey of Low-Burn-Rate Solid Rocket Propellants,” *Innovative Energetic Materials: Properties, Combustion Performance and Application*, Springer, Singapore, 2020, pp. 313–349. https://doi.org/10.1007/978-981-15-4831-4_11
- [6] Vernacchia, M. T., Mathesius, K. J., and Hansman, R. J., “Low-Thrust Solid Rocket Motors for Small, Fast Aircraft Propulsion: Design and Development,” *Journal of Propulsion and Power*, Vol. 38, No. 1, 2022, pp. 122–134. <https://doi.org/10.2514/1.B38104>
- [7] Vernacchia, M. T., Mathesius, K. J., and Hansman, R. J., “Slow-Burn Ammonium Perchlorate Propellants with Oxamide: Burn Rate Model, Testing, and Applications,” *Journal of Propulsion and Power*, Vol. 37, No. 5, 2021, pp. 792–800. <https://doi.org/10.2514/1.B38106>
- [8] Avital, G., Cohen, Y., Gamss, L., Kanelbaum, Y., Macales, J., Trieman, B., Yaniv, S., Lev, M., Stricker, J., and Sternlieb, A., “Experimental and Computational Study of Infrared Emission from Underexpanded Rocket Exhaust Plumes,” *Journal of Thermophysics and Heat Transfer*, Vol. 15, No. 4, 2001, pp. 377–383. <https://doi.org/10.2514/2.6629>
- [9] Wang, W., Li, S., Zhang, Q., and Wang, N., “Infrared Radiation Signature of Exhaust Plume from Solid Propellants with Different Energy Characteristics,” *Chinese Journal of Aeronautics*, Vol. 26, No. 3, 2013, pp. 594–600. <https://doi.org/10.1016/j.cja.2013.04.019>
- [10] Stowe, R., Ringuette, S., Fournier, P., Smithson, T., Pimentel, R., Alexander, D., and Link, R., “Effect of Flight and Motor Operating Conditions on IR Signature Predictions of Rocket Exhaust Plumes,” *International Journal of Energetic Materials and Chemical Propulsion*, Vol. 14, No. 1, 2015, pp. 29–56. <https://doi.org/10.1615/IntJEnergeticMaterialsChemProp.2015011502>
- [11] Kim, S., Kim, S., Kim, M., Song, S., and Lee, J. S., “Infrared Signature of NEPE, HTPB Rocket Plume Under Varying Flight Conditions and Motor Size,” *Infrared Physics & Technology*, Vol. 112, Jan. 2021, Paper 103590. <https://doi.org/10.1016/j.infrared.2020.103590>
- [12] Rudman, S., and Hibbeln, B. A., “Scaling of Optically Thick Plume Signatures,” *2000 IEEE Aerospace Conference. Proceedings*, Vol. 3, 2000, Inst. of Electrical and Electronics Engineers, New York, pp. 265–270. <https://doi.org/10.1109/AERO.2000.879854>
- [13] Mathesius, K. J., “Integrated Design of Solid Rocket Powered Vehicles Including Exhaust Plume Radiant Emission,” Ph.D. Thesis, Massachusetts Inst. of Technology, Cambridge, MA, 2023, <https://dspace.mit.edu/handle/1721.1/151348>.
- [14] Mathesius, K. J., and Hansman, R. J., “End-to-End Differentiable Model for Optimization of Rocket Powered Vehicles Including Exhaust Plume Radiant Emission,” *Journal of Spacecraft and Rockets*, 2023 (Manuscript Submitted for Publication).
- [15] Ponomarenko, A., “RPA: Tool for Liquid Propellant Rocket Engine Analysis,” 2010, http://www.propulsion-analysis.com/downloads/pub/RPA_LiquidRocketEngineAnalysis_II.pdf.
- [16] Mathesius, K. J., “Manufacturing Methods for a Solid Rocket Motor Propelling a Small, Fast Flight Vehicle,” SM Thesis, Massachusetts Inst. of Technology, Cambridge, MA, 2019, <https://dspace.mit.edu/handle/1721.1/122377>.
- [17] Vernacchia, M. T., “Development of Low-Thrust Solid Rocket Motors for Small, Fast Aircraft Propulsion,” Ph.D. Thesis, Massachusetts Inst. of Technology, Cambridge, MA, 2020, <https://dspace.mit.edu/handle/1721.1/127069>.
- [18] Simmons, F. S., *Rocket Exhaust Plume Phenomenology*, Aerospace Press, El Segundo, CA, 2000, pp. 39–42. <https://doi.org/10.2514/4.989087>

A. Dufrene
Associate Editor